Direct Synthesis of 7 nm-Thick Zinc(II)−Benzimidazole−Acetate Metal−Organic Framework Nanosheets

Feng Xue,[†] Prashant Kumar,[†] Wenqian Xu,[‡] K. Andre Mkhoyan,[†] and Michael Tsapatsis*,[†]

[†]Department of Chemical Engineering and Materials Science, University of Minnesota, Minneapolis, Minnesota 55455, United States
[‡]X-ray Science Division, Advanced Photon Source, Argonne National Laboratory, Lemont, Illinois 60439, United States

S *Supporting Information*

Metal−organic frameworks (MOFs) are crystalline porous materials consisting of metal ions or clusters connected by bridging organic ligands.[1,2] They have regularly arranged pores, tunable pore sizes and functionalities based on a diverse range of inorganic and organic building blocks that can be used.[3,4] These unique features make MOFs promising candidates in gas storage, separations and catalysis.[5−10] As with other materials, the ability to control crystal size and morphology is essential for enabling optimal use in such applications.[11−14] More specifically, MOF nanosheets with few-nanometer thickness and large lateral dimensions, hold promise for ultraselective highly permeable gas separation membranes because molecularly sized pores oriented perpendicular to the basal plane can ensure the desirable separation selectivity and increased permeance along their thin dimension.[15−18] For the preparation of nanosheet-based membranes, it is a critical prerequisite to obtain a stable suspension containing crystalline nanosheets with uniform thickness and high aspect ratio.[19,20] However, it remains challenging to synthesize stable MOF nanosheet suspensions satisfying these requirements.

Similar to other nanosheets, MOF nanosheets can be fabricated by two approaches. The top-down approach involves delamination of layered MOF precursors via methods such as sonication and chemical intercalation.[21−25] This approach is simple but the obtained nanosheets often suffer from structural deterioration, fragmentation and aggregation. Moreover, this approach has often a low yield and does not offer good control over the morphology of nanosheets. The direct (bottom-up) synthesis of MOF nanosheets is more desirable but relies on our ability to direct crystal growth to form high-aspect-ratio nanosheets at reasonable yield. Apart from few recent reports on zeolitic imidazolate framework nanosheets,[26,27] there are only two series of MOFs that could be directly synthesized as discrete ultrathin nanosheets dispersible in solvents.[17,28] Rodenas et al. reported a three-layer synthesis method for M-BDC (M = Cu, Co, BDC = 1,4-benzenedicarboxylate) nanosheets by modulating the growth kinetics of MOF crystals.[17] The obtained nanosheets were successfully applied for the fabrication of CO_2-selective MOF-polymer composite membranes. Zhao et al. introduced a polymer as surfactant in the synthesis of M-TCPP (M = Zn, Cu, Cd, Co, TCPP = tetrakis (4-carboxyphenyl)porphyrin) nanosheets.[28] They proposed that the attachment of surfactant on the MOF surface restricts the thermodynamically favored layer-stacking growth and helps to stabilize the nanosheets, yielding high-aspect-ratio nanosheets with sub-10 nm thickness. In order for

these nanosheets to be used for membrane applications, the polymer surfactant should probably have to be removed.

Here we report the direct synthesis of dispersible Zn(Bim)-OAc (Bim = benzimidazole, OAc = acetate) MOF nanosheets. Zn(Bim)OAc and its isostructural counterpart Co(Bim)OAc were originally reported in the form of bulk materials.[29,30] Later, a lamellar structure consisting of Zn(Bim)OAc interleaved with cethyltrimethylammonium bromide (CTAB) was reported by Lotsch and co-workers. However, exfoliation of the lamellar structure in organic solvents resulted mainly in anisotropic nanobelts. Moreover, the nanobelts contain CTAB surfactant.[24] With the direct synthesis method reported here, ultrathin Zn(Bim)OAc nanosheets are produced without fragmentation. Furthermore, it is demonstrated that synthesis temperature is critical to tuning the morphology of the nanostructure from nanobelts to nanosheets. We also demonstrate the formation of oriented deposits and the removal of the surfactant via a heat treatment. This work paves the way toward evaluation of Zn(Bim)OAc for membrane applications.

The structure of Zn(Bim)OAc as proposed in ref 29 is shown in Figure 1a. Two-dimensional (2D) layers are stacked along the *a* axis due to van der Waals forces. Within the 2D layer, each Zn ion is coordinated with two benzimidazole ligands and two acetate ligands in a distorted tetrahedral geometry, and each benzimidazole and acetate connect with two Zn ions. Interestingly, all the Zn−benzimidazole−Zn (Zn-Bim-Zn) linkages are along the *b* axis whereas all the Zn−acetate−Zn (Zn-OAc-Zn) linkages are along the *c* axis. Their crossing creates four-membered ring within the layer, with an aperture size that can be estimated from crystallographic data to be ∼2.4 Å. Following the conventional solvothermal synthesis protocol reported in ref 24, plate-like MOF crystals with lateral size ranging from 100 nm to 12 μm were obtained, some of which are grown together, forming irregularly shaped particles (Supporting Information, Figure S1).

Following ref 24, CTAB is introduced to regulate the crystal nucleation and growth. As a cationic surfactant, CTAB has been proposed to selectively attach to basal crystal planes to enable anisotropic growth of Zn(Bim)OAc and other MOFs[31] in a controlled manner. The presence of the CTAB hydrophobic tail on the crystal surface could also stabilize it and prevent lamellar stacking by dispersing the nanosheets in solvents with
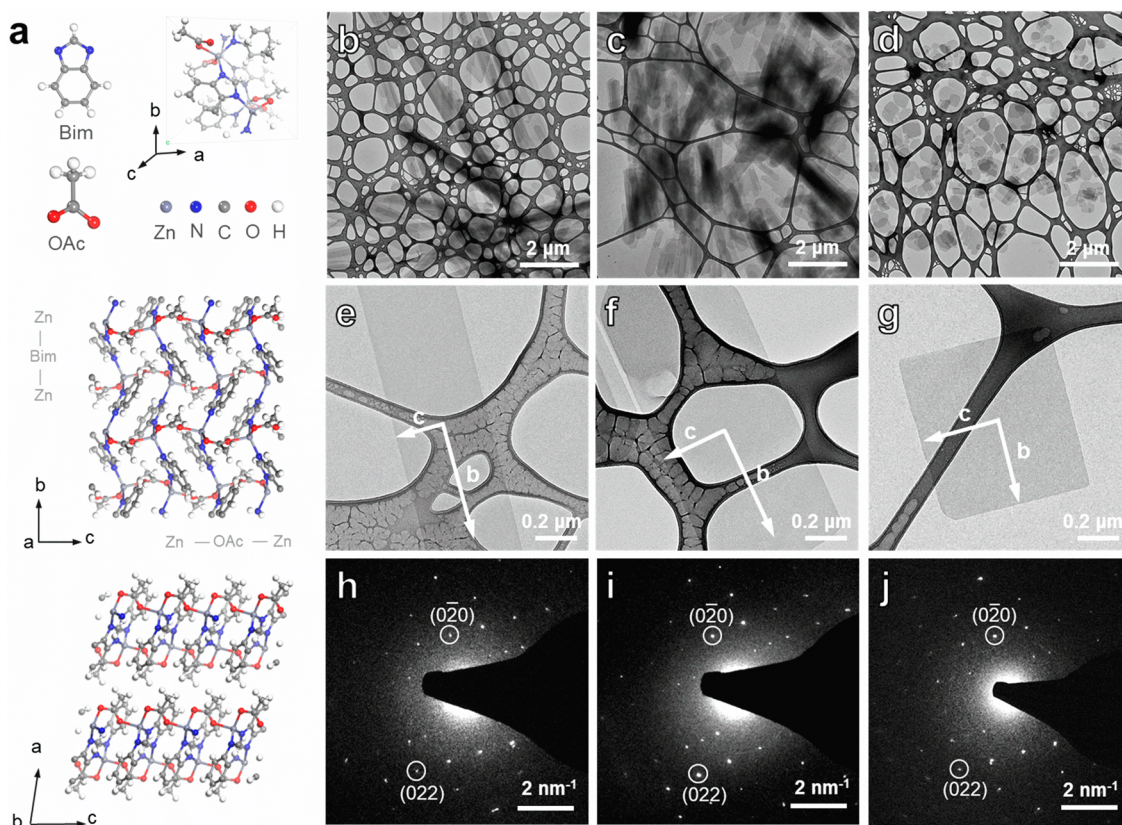
Figure 1. (a) Building units and the corresponding unit cell of Zn(Bim)OAc structure (top), 2D layers are viewed along the *a* axis (middle) and along the *b* axis (bottom). Structure of a single layer features Zn-Bim-Zn linkage along the *b* axis and Zn-OAc-Zn linkage along the *c* axis. TEM images of several nanocrystals, single nanocrystal and its corresponding electron diffraction pattern for synthesis of Zn(Bim)OAc structure at (b,e,h) 110 °C, (c,f,i) 60 °C and (d,g,j) 25 °C.
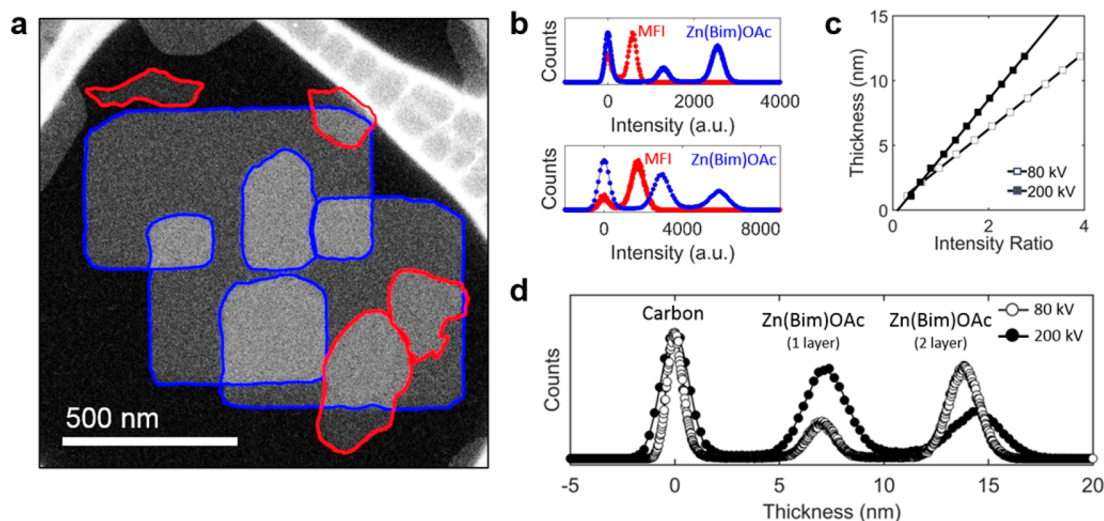
Figure 2. (a) HAADF-STEM image obtained at 80 kV of Zn(Bim)OAc nanosheet (outlined in blue) and 3.2 nm-thick 2D MFI (outlined in red) dispersed on an amorphous carbon support. (b) Intensity distribution in HAADF-STEM images of 3.2 nm-thick 2D MFI and Zn(Bim)OAc nanosheet acquired under similar TEM conditions at 80 kV (top) and 200 kV (bottom). (c) Calibration curves generated through HAADF-STEM simulation to convert intensity distribution in the image to thickness. (d) Intensity distribution of Zn(Bim)OAc nanosheet shown in panel b is converted to thickness distribution after applying the conversion shown in panel c. The single layer Zn(Bim)OAc nanosheet thickness is calculated to be 7.0 nm ± 0.5 nm at 80 kV and 7.2 nm ± 1.7 nm at 200 kV.

which CTAB has favorable interactions. The synthesis was first carried out for 16 h at 110 °C which is slightly higher than the 100 °C temperature reported in ref 24. The bright-field transmission electron microscopy (TEM) images (Figures 1b,e) reveal the morphology of the product to be ultrathin nanobelts with average lateral dimensions of 300 nm (width) and 4 um (length). The selected-area electron diffraction (SAED) pattern (Figure 1h) recorded along the [100] zone of

Zn(Bim)OAc exhibits (0kl) reflections. According to the SAED pattern, we determined the lateral dimensions of the nanobelt to correspond to the b and c axes of Zn(Bim)OAc.

It is known that temperature can affect the crystal growth rates and here we hypothesized that the growth rates along the Zn-Bim-Zn vs Zn-OAc-Zn chains could have different temperature dependence. Indeed, when the temperature was reduced, the thin nature of the product was retained while the ratio between the long and short lateral dimensions kept decreasing, with average ratio of 5.7 when synthesized at 60 °C (Figures 1c,f), and 1.3 when synthesized at room temperature (Figures 1d,g). To understand the temperature-dependent morphology change, we investigated its relationship with the crystal structure by SAED. As shown in Figures 1e−j, the long axis of the belt-like crystals was determined to be the b axis (Zn-Bim-Zn chain) of Zn(Bim)OAc, and the short axis of the belt-like crystals was determined to be the c axis (Zn-OAc-Zn chain) of Zn(Bim)OAc. Since the two axes correspond to two different linkages, the shape variation may result from the change in relative linker addition rate to metal center. At high temperature, the addition of benzimidazole to Zn center apparently happens much faster than the addition of acetate to Zn center, resulting in nanobelt growing favorably along the b axis. With decreasing temperature, the addition rate of benzimidazole drops and becomes comparable to the addition rate of acetate at room temperature. As a result, ultrathin nanosheets with an average lateral dimension of 600 nm were successfully prepared at room temperature.

To determine the thickness of nanosheets, a high-angle annular dark-field scanning transmission electron microscopy (HAADF-STEM) based method was developed. Image intensity in a HAADF-STEM image is typically proportional to Z^{α}, (α = 1.3−2.0), where average Z is the atomic number of the specimen through which electron beam passes.[32−35] Therefore, we utilized this inherent property of HAADF-STEM imaging to determine the thickness of a material with known composition by calibrating it with a standard material of known thickness and composition. For standard, we used the 3.2 nm-thick zeolite MFI nanosheets reported in ref 19. Figure 2a shows the HAADF-STEM image of Zn(Bim)OAc (outlined in blue) and 3.2 nm-thick zeolite MFI nanosheets (outlined in red) deposited on an amorphous carbon support. HAADF intensity distributions from two different images (Figure S2) acquired under similar TEM conditions at 80 and 200 kV (Figure 2b) were obtained and analyzed. According to the calibration curves generated through HAADF-STEM simulation (Figures 2c and S3), the intensity distribution of Zn(Bim)OAc nanosheets shown in Figure 2b was converted to the thickness distribution as shown in Figure 2d. Single Zn(Bim)OAc nanosheet displays a thickness of 7.0 nm ± 0.5 nm at 80 kV and 7.2 nm ± 1.7 nm at 200 kV, which corresponds to a stack of six to seven two-dimensional Zn(Bim)OAc layers. This result is consistent with the thickness measurement by atomic force microscopy (AFM), where the single layer nanosheet thickness is in the range of 7−9 nm (Figure S4).

In order to further study the crystal structure of nanosheets, X-ray diffraction (XRD) measurements were performed. The powder X-ray diffraction pattern (PXRD, Figure S5) confirms the presence of Zn(Bim)OAc in the sample, as the high-angle peaks ($2\theta > 11°$) match the simulated pattern of Zn(Bim)OAc based on the structure reported in ref 29. However, the peak positions are shifted to lower angles. Moreover, in the low-

angle region ($2\theta < 11°$), two intense peaks as well as several small peaks appear, which do not correspond to the reported structure of Zn(Bim)OAc in ref 29. These peaks were also reported in ref 24 and were attributed to a lamellar structure with a lattice period of around 8 nm. Within the lamellar structure, CTAB is sandwiched between the stacked nanosheets at periodic locations.[24] As described next, we identified calcination conditions that remove the surfactant and the resulting material exhibits XRD pattern in close agreement with CTAB-free Zn(Bim)OAc.

Because the surfactant may block transport of molecules in membrane applications, it is desirable to have it removed. To identify conditions to remove CTAB without altering the structure of Zn(Bim)OAc, thermogravimetric analysis (TGA) was performed. As shown in Figure S6a, pure Zn(Bim)OAc (made without using CTAB) shows a sharp weight loss at temperatures higher than 400 °C whereas the nanosheets made with CTAB experience a gradual weight loss from 230 °C before a sharp weight loss takes place at 400 °C. Considering that the weight loss of pure CTAB happens at similar temperature (it starts at about 200 °C and reaches 95% at 330 °C), the initial gradual weight loss in as-synthesized nanosheets could be attributed to the decomposition of CTAB. Because the loss of CTAB appears to start before the decomposition of Zn(Bim)OAc, heat treatment for CTAB removal was attempted by holding the temperature at 325 °C under air flow for 15 h (Figure S6b). After the heat treatment, XRD of the product (Figure S6c) showed exclusively reflections from Zn(Bim)OAc. The peak broadening of (100) and (200) of nanosheet sample relative to its bulk counterpart confirms its thin nature. The additional peaks which do not correspond to Zn(Bim)OAc structure disappeared. This observation is consistent with the assignment of the extra XRD peaks in ref 24 to the presence of CTAB and indicates that the structure of Zn(Bim)OAc was retained while most of surfactant molecules were removed after the heat treatment, though a small amount of their counterion bromine was detected by energy-dispersive X-ray spectroscopy (EDS) (Table S2). To further confirm the CTAB removal, the residue weight percent of heat-treated nanosheets after full calcination to 700 °C was estimated, and compared with the residue mass acquired from TGA of CTAB-containing nanosheets. By assuming no surfactant presence in heat-treated nanosheets, a residue weight percent of 27.3% was calculated, which compares well with the 26.8% residue obtained from TGA (calculation is shown in Supporting Information).

The orientation of nanosheets, which determines the orientation of pore system with respect to the direction of permeate flow, is critical to the separation efficiency of nanosheet-based membranes. To demonstrate preferentially oriented coatings of Zn(Bim)OAc, we used Si wafers and a stamping method.[20,36−38] As illustrated in Figure 3a, the nanosheets dispersed in tetrahydrofuran (THF) were transferred to the air−water interface by applying small quantities of the suspension dropwise onto the water surface. THF dissolved in water or evaporated, leading to nanosheets spreading on the surface of water. The nanosheets were introduced to Si wafer by Langmuir−Schaefer type transfer and the obtained coating was characterized by scanning electron microscopy (SEM) and synchrotron in-plane XRD. Figure 3b shows a typical SEM image of the coating indicating that nanosheets lie flat on the substrate. The in-plane XRD of the coating (Figure 3c) shows exclusively reflections from (0kl) crystallographic planes of
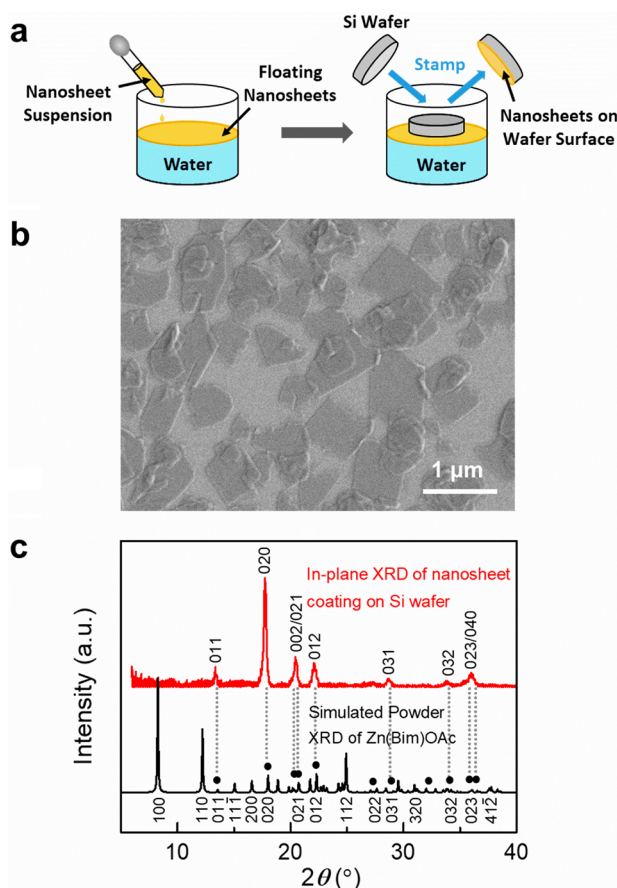
Figure 3. (a) Schematic of nanosheet coating process via stamping. (b) SEM image of nanosheet coating obtained by the stamping process. (c) In-plane XRD pattern of nanosheet coating on Si wafer (top) and simulated powder XRD pattern of Zn(Bim)OAc (bottom). The (0kl) peaks are marked with dots in the simulated pattern.

Zn(Bim)OAc, indicative of the preferentially a-out-of-plane orientation.

In summary, we demonstrate that changing crystallization temperature can lead to direct synthesis of Zn(Bim)OAc nanosheets. Using HAADF-STEM, the thickness of Zn(Bim)-OAc nanosheet was determined to be 7 nm. Moreover, we identify a temperature window allowing to remove the CTAB surfactant associated with Zn(Bim)OAc layers and show that Zn(Bim)OAc nanosheets can be transferred from an air—water interface to form an oriented coating on Si wafer. The obtained nanosheets with high aspect ratio and uniform thickness may open new opportunities for their application as gas separation membranes and their synthesis approach holds promise to be extended to other MOF structures to realize tunable porosity and functionality of MOF nanosheets.

ASSOCIATED CONTENT

Ⓢ Supporting Information

The Supporting Information is available free of charge on the ACS Publications website at DOI: 10.1021/acs.chemmater.7b04083.

Synthetic procedures, characterization methods and additional data (PDF)

AUTHOR INFORMATION

Corresponding Author

*M. Tsapatsis. E-mail: tsapatsis@umn.edu.

ORCID Ⓘ

K. Andre Mkhoyan: 0000-0003-3568-5452

Michael Tsapatsis: 0000-0001-5610-3525

Notes

The authors declare no competing financial interest.

REFERENCES

(1) Yaghi, O. M.; O'Keeffe, M.; Ockwig, N. W.; Chae, H. K.; Eddaoudi, M.; Kim, J. Reticular synthesis and the design of new materials. *Nature* **2003**, *423*, 705−714.

(2) Zhou, H.-C.; Long, J. R.; Yaghi, O. M. Introduction to metal-organic frameworks. *Chem. Rev.* **2012**, *112*, 673−674.

(3) Furukawa, H.; Cordova, K. E.; O'Keeffe, M.; Yaghi, O. M. The chemistry and applications of metal-organic frameworks. *Science* **2013**, *341*, 1230444.

(4) Deria, P.; Mondloch, J. E.; Karagiaridi, O.; Bury, W.; Hupp, J. T.; Farha, O. K. Beyond post-synthesis modification: evolution of metal—organic frameworks via building block replacement. *Chem. Soc. Rev.* **2014**, *43*, 5896−5912.

(5) Li, J.-R.; Kuppler, R. J.; Zhou, H.-C. Selective gas adsorption and separation in metal—organic frameworks. *Chem. Soc. Rev.* **2009**, *38*, 1477−1504.

(6) Qiu, S.; Xue, M.; Zhu, G. Metal-organic framework membranes: from synthesis to separation application. *Chem. Soc. Rev.* **2014**, *43*, 6116−6140.

(7) Lee, J.; Farha, O. K.; Roberts, J.; Scheidt, K. A.; Nguyen, S. T.; Hupp, J. T. Metal−organic framework materials as catalysts. *Chem. Soc. Rev.* **2009**, *38*, 1450−1459.

(8) Pan, Y.; Li, T.; Lestari, G.; Lai, Z. Effective separation of propylene/propane binary mixtures by ZIF-8 membranes. *J. Membr. Sci.* **2012**, *390−391*, 93−98.

(9) Kwon, H. T.; Jeong, H.-K. In situ synthesis of thin zeolitic−imidazolate framework ZIF-8 membranes exhibiting exceptionally high propylene/propane separation. *J. Am. Chem. Soc.* **2013**, *135*, 10763−10768.

(10) Brown, A. J.; Brunelli, N. A.; Eum, K.; Rashidi, F.; Johnson, J. R.; Koros, W. J.; Jones, C. W.; Nair, S. Interfacial microfluidic processing of metal-organic framework hollow fiber membranes. *Science* **2014**, *345*, 72−75.

(11) Stock, N.; Biswas, S. Synthesis of metal-organic frameworks (MOFs): routes to various MOF topologies, morphologies, and composites. *Chem. Rev.* **2012**, *112*, 933−969.

(12) De Yoreo, J. J.; Gilbert, P. U. P. A.; Sommerdijk, N. A. J. M.; Penn, R. L.; Whitelam, S.; Joester, D.; Zhang, H.; Rimer, J. D.; Navrotsky, A.; Banfield, J. F.; Wallace, A. F.; Michel, F. M.; Meldrum, F. C.; Cölfen, H.; Dove, P. M. Crystallization by particle attachment in

synthetic, biogenic, and geologic environments. *Science* **2015**, *349*, aaa6760.

(13) Snyder, M. A.; Tsapatsis, M. Hierarchical nanomanufacturing: From shaped zeolite nanoparticles to high-performance separation membranes. *Angew. Chem., Int. Ed.* **2007**, *46*, 7560−7573.

(14) Ogino, I.; Eilertsen, E. A.; Hwang, S.-J.; Rea, T.; Xie, D.; Ouyang, X.; Zones, S. I.; Katz, A. Heteroatom-tolerant delamination of layered zeolite precursor materials. *Chem. Mater.* **2013**, *25*, 1502−1509.

(15) Kim, W.-g.; Nair, S. Membranes from nanoporous 1D and 2D materials: A review of opportunities, developments, and challenges. *Chem. Eng. Sci.* **2013**, *104*, 908−924.

(16) Peng, Y.; Li, Y.; Ban, Y.; Jin, H.; Jiao, W.; Liu, X.; Yang, W. Metal-organic framework nanosheets as building blocks for molecular sieving membranes. *Science* **2014**, *346*, 1356−1359.

(17) Rodenas, T.; Luz, I.; Prieto, G.; Seoane, B.; Miro, H.; Corma, A.; Kapteijn, F.; i Xamena, F. X. L.; Gascon, J. Metal-organic framework nanosheets in polymer composite materials for gas separation. *Nat. Mater.* **2015**, *14*, 48−55.

(18) Wang, X.; Chi, C.; Zhang, K.; Qian, Y.; Gupta, K. M.; Kang, Z.; Jiang, J.; Zhao, D. Reversed thermo-switchable molecular sieving membranes composed of two-dimensional metal-organic nanosheets for gas separation. *Nat. Commun.* **2017**, *8*, 14460.

(19) Varoon, K.; Zhang, X.; Elyassi, B.; Brewer, D. D.; Gettel, M.; Kumar, S.; Lee, J. A.; Maheshwari, S.; Mittal, A.; Sung, C.-Y.; Cococcioni, M.; Francis, L. F.; McCormick, A. V.; Mkhoyan, K. A.; Tsapatsis, M. Dispersible exfoliated zeolite nanosheets and their application as a selective membrane. *Science* **2011**, *334*, 72−75.

(20) Jeon, M. Y.; Kim, D.; Kumar, P.; Lee, P. S.; Rangnekar, N.; Bai, P.; Shete, M.; Elyassi, B.; Lee, H. S.; Narasimharao, K.; Basahel, S. N.; Al-Thabaiti, S.; Xu, W.; Cho, H. J.; Fetisov, E. O.; Thyagarajan, R.; DeJaco, R. F.; Fan, W.; Mkhoyan, K. A.; Siepmann, J. I.; Tsapatsis, M. Ultra-selective high-flux membranes from directly synthesized zeolite nanosheets. *Nature* **2017**, *543*, 690−694.

(21) Amo-Ochoa, P.; Welte, L.; González-Prieto, R.; Sanz Miguel, P. J.; Gómez-García, C. J.; Mateo-Marti, E.; Delgado, S.; Gómez-Herrero, J.; Zamora, F. Single layers of a multifunctional laminar Cu (I, II) coordination polymer. *Chem. Commun.* **2010**, *46*, 3262−3264.

(22) Li, P.-Z.; Maeda, Y.; Xu, Q. Top-down fabrication of crystalline metal−organic framework nanosheets. *Chem. Commun.* **2011**, *47*, 8436−8438.

(23) Gallego, A.; Hermosa, C.; Castillo, O.; Berlanga, I.; Gómez-García, C. J.; Mateo-Martí, E.; Martínez, J. I.; Flores, F.; Gómez-Navarro, C.; Gómez-Herrero, J.; Delgado, S.; Zamora, F. Solvent-induced delamination of a multifunctional two dimensional coordination polymer. *Adv. Mater.* **2013**, *25*, 2141−2146.

(24) Junggeburth, S. C.; Diehl, L.; Werner, S.; Duppel, V.; Sigle, W.; Lotsch, B. V. Ultrathin 2D coordination polymer nanosheets by surfactant-mediated synthesis. *J. Am. Chem. Soc.* **2013**, *135*, 6157−6164.

(25) Ding, Y.; Chen, Y.-P.; Zhang, X.; Chen, L.; Dong, Z.; Jiang, H.-L.; Xu, H.; Zhou, H.-C. Controlled intercalation and chemical exfoliation of layered metal−organic frameworks using a chemically labile intercalating agent. *J. Am. Chem. Soc.* **2017**, *139*, 9136−9139.

(26) Jiang, Y.; Liu, H.; Tan, X.; Guo, L.; Zhang, J.; Liu, S.; Guo, Y.; Zhang, J.; Wang, H.; Chu, W. Monoclinic ZIF-8 Nanosheet-Derived 2D Carbon Nanosheets as Sulfur Immobilizer for High-Performance Lithium Sulfur Batteries. *ACS Appl. Mater. Interfaces* **2017**, *9*, 25239−25249.

(27) Huang, L.; Zhang, X.; Han, Y.; Wang, Q.; Fang, Y.; Dong, S. In situ synthesis of ultrathin metal−organic framework nanosheets: a new method for 2D metal-based nanoporous carbon electrocatalysts. *J. Mater. Chem. A* **2017**, *5*, 18610−18617.

(28) Zhao, M.; Wang, Y.; Ma, Q.; Huang, Y.; Zhang, X.; Ping, J.; Zhang, Z.; Lu, Q.; Yu, Y.; Xu, H.; Zhao, Y.; Zhang, H. Ultrathin 2D metal−organic framework nanosheets. *Adv. Mater.* **2015**, *27*, 7372−7378.

(29) Li, X.-M. Poly[μ2-acetato-μ2-benzimidazolato-zinc(II)]. *Acta Crystallogr., Sect. E: Struct. Rep. Online* **2007**, *63*, m1984−m1984.

(30) Arai, L.; Nadeem, M. A.; Bhadbhade, M.; Stride, J. A. A 2D cobalt based coordination polymer constructed from benzimidazole and acetate ion exhibiting spin-canted antiferromagnetism. *Dalton Trans.* **2010**, *39*, 3372−3374.

(31) Flügel, E. A.; Aronson, M. T.; Junggeburth, S. C.; Chmelka, B. F.; Lotsch, B. V. Surfactant-directed syntheses of mesostructured zinc imidazolates: formation mechanism and structural insights. *CrystEngComm* **2015**, *17*, 463−470.

(32) Kirkland, E. J.; Loane, R. F.; Silcox, J. Simulation of annular dark field STEM images using a modified multislice method. *Ultramicroscopy* **1987**, *23*, 77−96.

(33) Pennycook, S. J. Z-contrast STEM for materials science. *Ultramicroscopy* **1989**, *30*, 58−69.

(34) Wang, Z. W.; Li, Z. Y.; Park, S. J.; Abdela, A.; Tang, D.; Palmer, R. E. Quantitative Z-contrast imaging in the scanning transmission electron microscope with size-selected clusters. *Phys. Rev. B: Condens. Matter Mater. Phys.* **2011**, *84*, 073408.

(35) Odlyzko, M. L.; Held, J. T.; Mkhoyan, K. A. Atomic bonding effects in annular dark field scanning transmission electron microscopy. II. Experiments. *J. Vac. Sci. Technol., A* **2016**, *34*, 041603.

(36) Rangnekar, N.; Shete, M.; Agrawal, K. V.; Topuz, B.; Kumar, P.; Guo, Q.; Ismail, I.; Alyoubi, A.; Basahel, S.; Narasimharao, K.; Macosko, C. W.; Mkhoyan, K. A.; Al-Thabaiti, S.; Stottrup, B.; Tsapatsis, M. 2D zeolite coatings: Langmuir−Schaefer deposition of 3 nm thick MFI zeolite nanosheets. *Angew. Chem., Int. Ed.* **2015**, *54*, 6571−6575.

(37) Makiura, R.; Motoyama, S.; Umemura, Y.; Yamanaka, H.; Sakata, O.; Kitagawa, H. Surface nano-architecture of a metal−organic framework. *Nat. Mater.* **2010**, *9*, 565−571.

(38) Imperiali, L.; Liao, K.-H.; Clasen, C.; Fransaer, J.; Macosko, C. W.; Vermant, J. Interfacial rheology and structure of tiled graphene oxide sheets. *Langmuir* **2012**, *28*, 7990−8000.